CHEMISTRY OF MATERIALS

pubs.acs.org/cm

Article

Functionalization of Electrode Surfaces with Reactive Supramolecular Oligomers Enables the Control of Monolayer Properties to Restore Electrochemical Reversibility

Ifigeneia Tsironi, Jarek A. Maleszka, Robert S. Wilson-Kovacs, Victor A. Paulino, Orlando Acevedo, Arindam Mukhopadhyay,* and Jean-Hubert Olivier*

Cite This: *Chem. Mater.* 2023, 35, 6877−6888

Read Online

ACCESS | Metrics & More | Article Recommendations | Supporting Information

ABSTRACT: The functionalization of conducting silicon (Si) substrates with redox-active probes delivers hybrid semiconducting interfaces whose electronic functions are parameterized by the molecular conformations of monolayers. However, it remains challenging to build electronically homogeneous semiconducting interfaces using flat, π-conjugated derivatives that are prone to aggregation, as structural heterogeneity in the solid state unequivocally engenders ill-defined electronic domains. This limitation has notoriously hampered the development of n-type semiconducting Si interfaces derived from rylene dyes, which possess enticing applications in solar energy capture and conversion. Herein, this challenge is overcome by using supramolecular oligomers derived from reactive naphthalene diimide (NDI) units as structural templates to control the electrochemical response of semiconducting monolayers at Si interfaces. Specifically, conducting Si surfaces functionalized with NDI noncovalent assemblies exhibit reversible electrochemical signals and reduction potentials stabilized by more than 100 mV compared to semiconducting interfaces derived from molecularly derived precursors. Leveraging density functional theory and molecular dynamics simulations, the potentiometric properties recorded experimentally are assigned to discrete NDI conformations, which are parameterized by the aggregation state of the precursors in solution. These findings delineate a novel strategy to control the electronic structure homogeneity of semiconducting interfaces constructed from dyes infamously known to form ill-defined electronic domains.

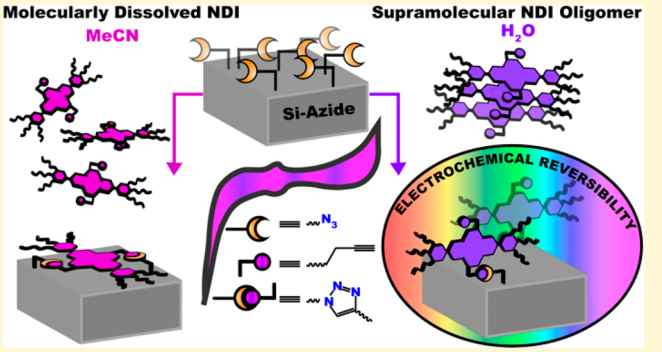

INTRODUCTION

Interfacing electroactive molecules with (semi)conducting substrates is critical to engineering hybrid functional materials relevant to solar energy capture and conversion, quantum information processing, and sensing.[1−10] In this regard, π-conjugated chromophores covalently anchored on hydrogen-terminated monocrystalline silicon (Si−H) surfaces delineate structurally well-defined and robust electro- and photoactive Si−organic hybrid nanointerfaces.[11−13] These platforms have enabled the interrogation of fundamental charge transfer processes from and to metallic electrodes, the engineering of tunable interfacial dipoles relevant to photocatalysis, and the elucidations of charge transfer states for data storage applications.[14−17] Despite the unambiguous promises of these semiconducting hybrids, the formation of n-type interfaces on (semi)conducting substrates that exhibit discrete electronic states remains challenging due to the erratic interactions of n-type precursors.[18−21] This limitation hampers the development of interfacial p−n junctions, circuit elements, and the pioneering of model systems to investigate the interaction of electronic ground and excited states of anchored dyes with the Fermi level of (semi)conducting inorganic surfaces, such as those derived from silicon. Indeed, recent studies have demonstrated that triplet energy transfer processes from silicon quantum dots to anchored chromophores open new avenues in engineering hybrid materials for solar energy capture and conversion.[22,23]

The electronic structures of organic/inorganic interfaces are primarily dictated by the conformation of the redox-active modules on surfaces, including their lateral interactions.[12,24−28] These structure−function properties are derived from the covalent functionalization methods used to form such interfaces, which primarily leverage molecularly dissolved building blocks.[29−32] For example, anchoring ferrocene units

Received: May 15, 2023
Revised: July 12, 2023
Published: August 15, 2023

on Si electrodes produces densely packed monolayers where lateral electronic interactions between Fc probes have been elucidated using scanning electrochemical microscopy.[19,24] Furthermore, due to its sphere-shaped geometry, the redox-active ferrocene modules do not suffer from the erratic aggregation processes that are enforced by surface confinement effects. Consequently, monolayers derived from ferrocene enable the formation of well-defined electronic states, thus providing ideal, reversible signals over a wide range of scan rates. In contrast, the attachment of flat, π-conjugated chromophores on inorganic (semi)conducting surfaces is unavoidably accompanied by erratic intermolecular interactions between the polyaromatic surfaces, creating ill-defined electronic states that restrict the elucidation of energy and electron transfer processes.[33]

While the importance of parameterizing the conformation of π-conjugated chromophores on inorganic surfaces is unambiguous, strategies to functionalize the surface of electrodes and nanocrystals primarily capitalize on the use of molecularly dissolved building blocks.[34,35] This approach ultimately restrains the ability to control the orientation and interaction modes of anchored redox-active probes, which are solely governed by surface confinement effects. In other words, the high surface density of reactive precursors anchored on (semi)conducting electrodes regulates the interactions between π-conjugated species. We have recently demonstrated that the aggregation properties of naphthalene diimide (NDI) dyes can be harnessed to construct semiconducting Si nanointerfaces (Si-NDI) whose conduction band energies are intimately associated with the aggregation state of NDI precursors.[13] However, these hybrid platforms exhibit irreversible electrochemical signals originating from erratic electron transfer processes combined with structural perturbations of redox-active monolayers upon n-doping. Congruent with this current limitation, strategies to tailor the conformation of molecular monolayers on inorganic substrates are needed to construct n-type (semi)conducting nanointerfaces equipped with homogeneous electronic structures.

Short stacks composed of π-conjugated building blocks, referred to as supramolecular oligomers in the following text, are structurally well-defined noncovalent assemblies that can be leveraged as precursors to build semiconducting interfaces. Notably, supramolecular oligomers constructed from NDI chromophores are appealing classes of semiconducting materials due to their tunable redox properties over large potentiometric windows and broad spectral coverage.[36,37] Furthermore, the functionalization of NDI's bay regions enables the perturbation of the frontier molecular orbital energy, thereby providing an efficient synthetic handle to control the redox properties of nanointerfaces.[38−41] Herein, we report the use of NDI-derived supramolecular oligomers shown in Scheme 1 as reactive precursors to construct semiconducting interfaces, whose reversible electrochemical signals indicate the formation of a homogeneous chemical environment. Interrogating the structure of the reactive NDI supramolecular oligomers in solution using ground-state electronic absorption spectroscopy and 2-dimensional nuclear magnetic resonance experiments reveals that this noncovalent assembly exists, on average, as a trimer species in an aqueous environment. Molecular dynamics simulation is used to confirm that the reactive ethynyl fragments flanked on the NDI repeating units are exposed and accessible to react. Azide-functionalized conducting Si electrodes are reacted with the

Scheme 1. Schematic Illustration of the Two Distinct Pathways Utilized to Functionalize the Si Surface with Supramolecular NDI Oligomers Formed in H_2O and Individualized Monomeric NDI Building Blocks in CH_3CN

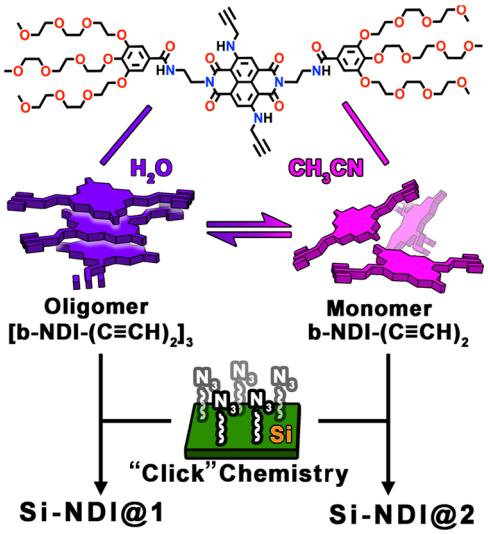

NDI supramolecular oligomer using click chemistry to deliver the semiconducting **Si-NDI@1** interface illustrated in Scheme 1. Compellingly, the reversible and reproducible cathodic signals ($E^{1/2}$ = −0.368 V *vs* Ag/AgCl (3M NaCl)) recorded at different scan rates confirm the successful covalent anchorage of the NDI redox probe at Si monolayer interfaces and indicate the formation of a homogeneous chemical environment and discrete electronic states. In sharp contrast, the **Si-NDI@2** nanointerface built from solvated building blocks (Scheme 1) exhibits more complex potentiometric properties and a cathodic shift of the NDI-centered reduction potential ($E^{1/2}$ = −0.474 V *vs* Ag/AgCl (3M NaCl)). Energy-minimized Si interfaces computed using density functional theory (DFT) provide insights into the diverging conformation adopted by NDI units in the two Si interfaces. While the redox probes in **Si-NDI@2** lay flat on the Si surface, the **Si-NDI@1** is characterized by NDI units whose conformations maximize interaction with the solvation environment. The combined experimental and theoretical results show that supramolecular architectures can be harnessed as conformational templates to imprint electronically homogeneous domains on surfaces. Our findings solve the long-standing challenge of constructing n-type semiconducting interfaces derived from flat, π-conjugated chromophores, which demonstrate reversible electrochemical processes.

RESULTS AND DISCUSSION

Supramolecular Oligomer Characterization. The amphiphilic NDI building block **b-NDI-(C≡CH)$_2$** shown in Scheme 1 forms supramolecular oligomers in an aqueous medium. While the terminal ethylene-oxide-derived side chains promote solubilization of the aggregated structures in water, the hydrophobic π-conjugated core flanked by propargyl amine side chains provides a synthetic handle to control not only the redox properties of the NDI dye, but it also enables the postassembly modification of the oligomers. An initial assessment of the ability of **b-NDI-(C≡CH)$_2$** units to assemble in water has been achieved using solvent-dependent ^{1}H NMR spectroscopy experiments. As shown in Figure S8C,

https://doi.org/10.1021/acs.chemmater.3c01168
Chem. Mater. 2023, 35, 6877−6888

increasing the ratio of D_2O in CD_3CN up to a ratio of 40:60 (v/v) has a negligible impact on the proton signals centered at 6.9 and 8.2 ppm. This observation suggests a minor perturbation of the chemical environment surrounding the NDI core. As the ratio of D_2O in CD_3CN is increased up to 100% D_2O, a drastic upfield shift of the aromatic protons is witnessed and concluded by the vanishing of the signals in a pure water environment.[42,43] These initial observations, along with the concomitant change in solution color from pink to blue (inset Figure S8A), suggest the formation of different species in pure water, which are subsequently investigated using ground-state electronic absorption spectroscopy.

Figure 1A highlights that in the 65:35 (v/v)CH_3CN/H_2O solvent mixture, the **b-NDI-(C≡CH)$_2$** construct exists under a

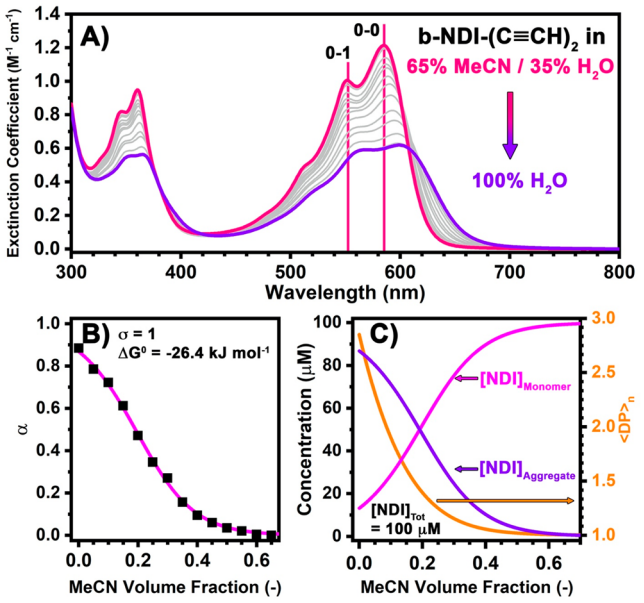

Figure 1. (A) Solvent-dependent UV−vis spectra that highlight the change of absorptive profile upon addition of water in acetonitrile solution; [NDI] = 100 μM. (B) Experimental degree of aggregation (square) calculated at 645 nm as a function of acetonitrile volume fraction. The best fit is shown in pink and corresponds to an isodesmic supramolecular polymerization mechanism. (C) Concentration profile of the different species, NDI as monomers and NDI comprised in aggregates as a function of the H_2O/CH_3CN solvent compositions.

molecularly dissolved state as confirmed by: (i) the 0-0, 0-1 vibronic transitions centered at 580 and 555 nm respectively, which are evenly separated by ∼160 meV, and (ii) the ratio of the 0-0 and 0-1 vibronic transitions which indicates the absence of inter- chromophoric interactions between NDI units.[44] As the ratio of CH_3CN in H_2O decreases, an overall decrease in the S_0 to S_1 oscillator strength is accompanied by a significant broadening of the visible absorption band concomitant with its bathochromic shift. These spectroscopic features indicate the formation of NDI-derived assemblies.[45−47] Using the change of absorptivity at 635, 640, 645, and 650 nm as fingerprints for the formation of noncovalent assembly, we plotted the degree of aggregation (α) as a function of CH_3CN volume fraction in water (Figure 1B). This relationship allows us to glean additional insights into the thermodynamic parameters that regulate the formation of the noncovalent assemblies using the supramolecular depolymerization approach introduced by Korevaar and Meijer and exploited by us and others to investigate the properties of water-soluble rylene dyes.[48−50] Refer to the Supporting Information for more details. Figure 1B shows that the best fit suggests a supramolecular (de)polymerization mechanism that is isodesmic and associated with an elongation equilibrium constant $K_e = 5.0 \times 10^4$ mol^{-1} in pure water. From this data, we can estimate that at a concentration of [NDI] = 100 μM, the building blocks exist as a small oligomer composed of an average of 3 repeating units, as highlighted in Figure 1C. In contrast to similar rylene-based building blocks that form supramolecular polymer following a nucleation-elongation mechanism in an aprotic solvent, the isodesmic growth mechanism elucidated for the **b-NDI-(C≡CH)$_2$** building block in water traces its origin from the inability of the NDI units to form dormant monomers. Indeed, the interaction of the amide-derived side chains with water molecules hampers the formation of intramolecular hydrogen bonds.[51,52]

To further confirm the existence of oligomeric species formed upon aggregation of the NDI building block in water, diffusion-ordered NMR spectroscopy (DOSY) was performed in differing ratios of deuterated acetonitrile and water at a concentration of [NDI] = 1 mM. Based on the acquired DOSY spectra shown in Figure S9, the diffusion coefficients are estimated to be 2.30×10^{-10} m^2/s in a 65:35 (v/v) CD_3CN/D_2O solution and 9.10×10^{-11} m^2/s in 100% D_2O. By relating the NDI's diffusion coefficients at 1 mM under molecularly dissolved and aggregated states, the number of repeating units can be estimated to be, on average, ∼12.5 units when fully assembled in water. Refer to Section 5 in the Supporting Information for more details on the calculations. The supramolecular polymerization parameters extracted from the UV−vis experimental data at a concentration of [NDI] = 1 mM predict an oligomer composed of 8 repeating units. The value calculated through DOSY analysis is similar, highlighting experimentally that the building block does indeed exist as a supramolecular oligomer in an aqueous medium.

Molecular Dynamics (MD) Simulations. To assess the structure of **b-NDI-(C≡CH)$_2$** dimeric and trimeric aggregates in solution, models of these aggregates water were simulated via the AMBER 18 software package. 200 ns constant NPT (Number of atoms, Pressure, Temperature) simulations confirmed the stability (and thus viability) of these states within this timeframe, revealing a morphology defined by rotationally offset, π-stacked aggregates with a width of 1.27 nm. Interestingly, the hydrophobic NDI termini of these aggregates were partially obscured by triethylene glycol (TEG) chains, reminiscent of findings from Syamala et al.[53]

The extent of this obscuring behavior was confirmed by population density mapping of the TEG chains over the course of these simulations, revealing that, at equilibrium, these chains occupied a high-density, axially focused "dumbbell-like" region for half of their simulations, with a more diffuse corona accounting for 80% of the total TEG chain atom counts across the simulation space (Figure 2). The number density of this axially focused region, ρ_{TEG}, is over 2.6 times higher than that of the diffuse region in the dimeric aggregate, the corresponding ratio in the trimeric aggregate was 2.45 times. Not only does this behavior, through partial obscuration of the NDI termini, account for the low elongation constant K_e and small oligomer scales at 100 μM discussed in the previous section, but it also exposes the propargyl bay substituents of **b-NDI-(C≡CH)$_2$**, rendering them free to react with the

https://doi.org/10.1021/acs.chemmater.3c01168
Chem. Mater. 2023, 35, 6877−6888

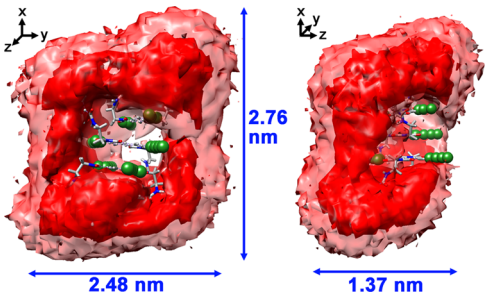

Figure 2. Representative structure (found via *K*-means clustering) of the trimer of **b-NDI-(C≡CH)$_2$** in water from the 200 ns simulation, with the propargyl bay substituents colored in green. Density mapping of the TEG chain oxygen and carbon atoms over the simulation yields the following isosurfaces: a high-density region (ρ > 216 counts Å^{-3}) in dark red which TEG chains occupy for 50% of the simulation time, and a low-density region (ρ > 44 counts Å^{-3}) which TEG chains occupy for 80% of the simulation time.

surrounding solution or adsorbing substrate. The contrast is especially stark for the trimeric species, whose face-to-face π-stacking between the NDI termini and the TEG-bearing phenyl moieties creates a highly defined TEG corona and a large exposed central pocket, the latter of which bears several propargyl groups which are available to facilitate postassembly modification of the aggregate.

Solid-State Morphologies. When drop cast from parent water or acetonitrile solutions, the NDI units exhibit vastly different solid-state morphologies, confirming that the building blocks exist in different aggregated states as a function of solvation environments. As seen in the atomic force microscopy images in Figure 3A, the supramolecular [**b-NDI-(C≡CH)$_2$**]$_3$ constructs evolve into isolated fibers which span microscale dimensions. Statistical analysis performed on height profiles recorded for 228 cross sections reveals the existence of superstructures with $d_{average}$ = 1.35 nm. Corroborating these thicknesses with the MD simulations discussed earlier, we posit that the 1.35 nm diameter constructs

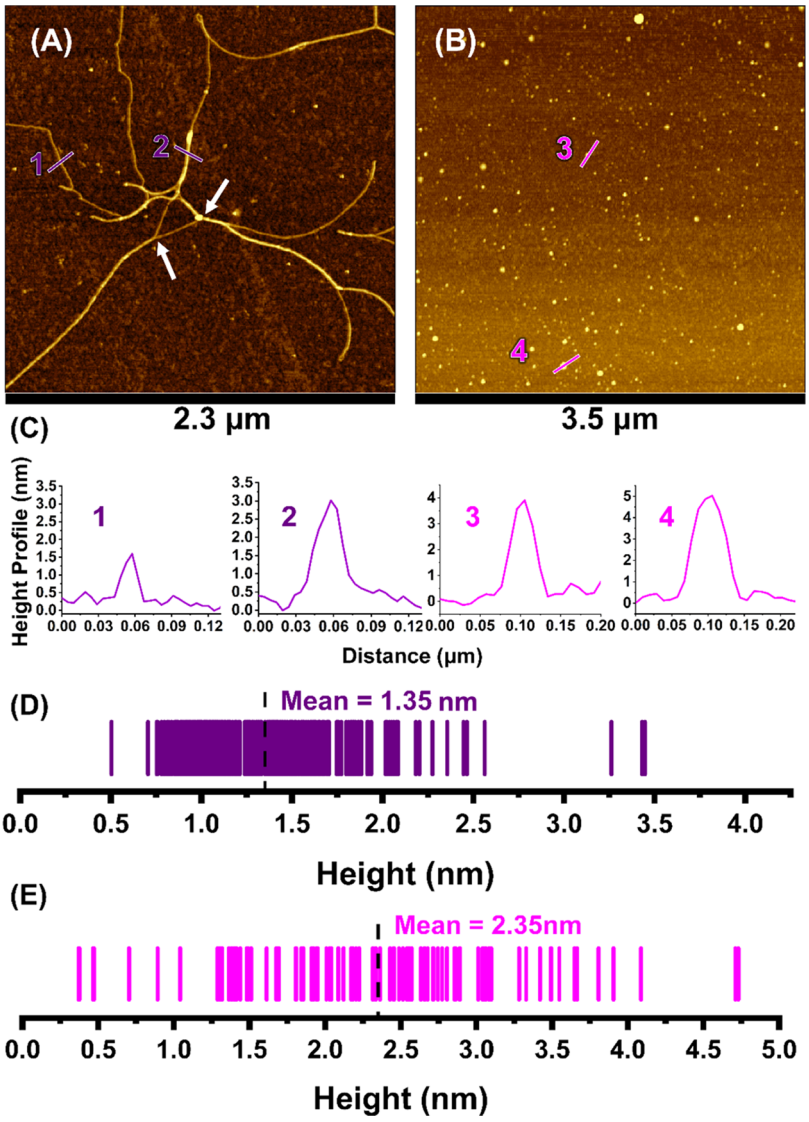

Figure 3. (A, B) Topographic intermittent contact mode atomic force microscopy (AFM) images that chronicle the solid-state morphology of **b-NDI-(C≡CH)$_2$** recorded for samples drop cast from the solutions of the latter in (A) neat H_2O and (B) dry CH_3CN on silicon (Si/SiO_x) substrate. (C) Associated height profile diagrams (left in H_2O and right in CH_3CN). (D-E) Statistical analysis of height profiles and size distribution (top, H_2O; bottom, CH_3CN).

https://doi.org/10.1021/acs.chemmater.3c01168
Chem. Mater. 2023, 35, 6877−6888

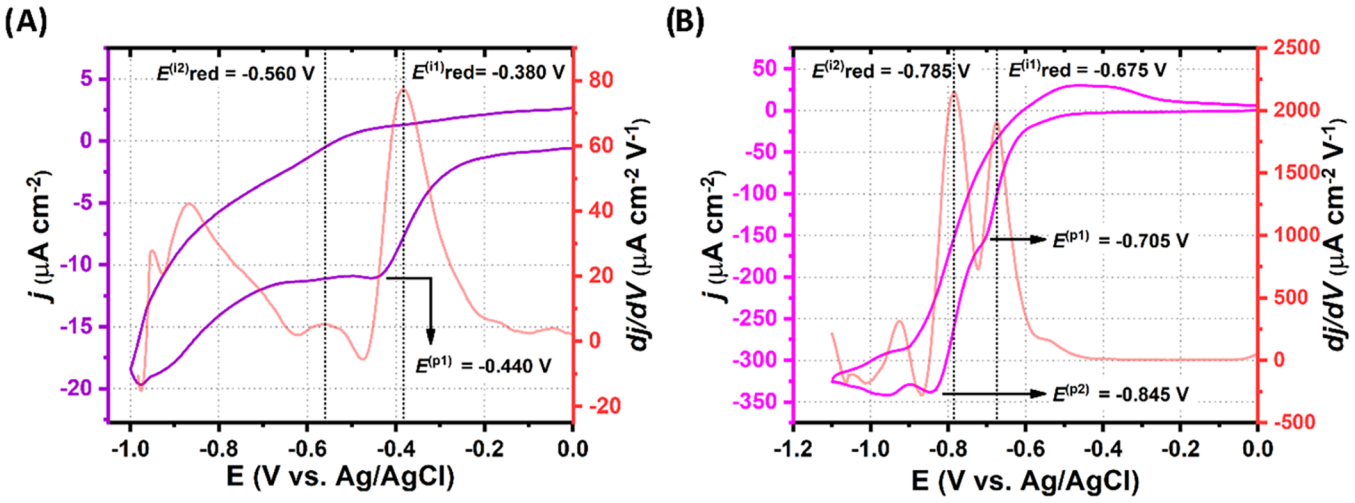

Figure 4. Cyclic voltammograms (scan rate = 25 mV s^{-1}) and their first derivative plots of **b-NDI-(C≡CH)$_2$** recorded for the solutions (concentration = 200 μM) in (A) H_2O (supporting electrolyte = 0.1 M NaCl) and (B) dry CH_3CN (supporting electrolyte = 0.1 M *n*-Bu_4NPF_6) under Ar at 25 °C. Note that the working, reference, and counter electrodes employed for the voltammetric measurements were glassy carbon (electroactive surface area = 0.071 cm^2), Ag/AgCl (3 M NaCl), and Pt wire, respectively.

correspond to NDI building blocks stacking along a one-dimensional axis. Evidently, thicker structures are produced by bundling. Indeed, the arrow-pointed spots in Figure 3A highlight regions where the merging of two elementary fibers (d = 1.35 nm) can be witnessed, forming thicker structures. We posit that the thicker structures are produced from the lateral interactions of the individualized fibers formed during the drop-casting steps. The increase in the concentration of the NDI supramolecular oligomers during solvent evaporation is accompanied by the formation of longer 1D aggregates whose short triethylene glycol side chains at the periphery of the rigid core promote noncovalent interactions between stacks.

In contrast, nanoparticles best describe the solid-state morphologies adopted by the solvated **b-NDI-(C≡CH)$_2$** building block in CH_3CN as shown in Figure 3B. Statistical analysis of 90 cross sections reveals a broad distribution of nanoparticle sizes with a mean diameter of 2.35 nm. The lack of hierarchical superstructures in CH_3CN solvent prevents the formation of the 1D superstructures witnessed by the water-soluble [**b-NDI-(C≡CH)$_2$**]$_3$ oligomer. We stress that the micrometer-long fibers observed by AFM are produced during the drop-casting of the supramolecular [**b-NDI-(C≡CH)$_2$**]$_3$ constructs, which evolve into larger hierarchical objects as the concentration increases during evaporation.

Potentiometric Properties of Solvated NDI Precursors. The (opto)electronic properties of the supramolecular construct [**b-NDI-(C≡CH)$_2$**]$_3$ and its parent, solubilized building block are investigated through cyclic voltammetry and spectroelectrochemistry experiments. To provide a comprehensive discussion, we highlight first some key potentiometric properties of the solvated NDI precursors in CH_3CN. The cyclic voltammetry experiments performed on the parent, molecularly dissolved precursors **b-NDI-(C≡CH)$_2$** are shown in Figure 4B. When sweeping toward a final cathodic potential of −1.000 V *vs* Ag/AgCl (3M NaCl), two electrochemical signals are diagnosed at $E^{(p1)}$ = −0.705 V and $E^{(p2)}$ = −0.845 V but appear irreversible when equilibrating the potential back to 0.000 V. A more accurate insight into the recorded potentiometric properties is derived by evaluating the first and second cathodic inflection potentials, $E_{red}^{(i1)}$ and $E_{red}^{(i2)}$, which are assessed by plotting the first derivative of the CVs when sweeping towards the cathodic side.[54] While at first glance, the calculated $E_{red}^{(i1)}$ = − 0.675 V and $E_{red}^{(i2)}$ = −0.785 V *vs* Ag/AgCl (3M NaCl) could be assigned to the first and second reduction of the NDI core, the formation of the dianion species $[NDI]^{2-}$ have been reported to occur at more negative cathodic potentials, e.g., ∼1.000 V *vs* Ag/AgCl (3M NaCl).[55] Spectroelectrochemistry experiments were performed to gain insights into the species formed under reductive conditions. The associated spectra are shown in Figure S14 and highlight the rise of a broad NIR transition band, which reaches the maximum intensity at a potential of −0.800 V *vs* Ag/AgCl. Planar rylene diimide anion derivatives are prone to form radical π-anion aggregates, as reported by us and others.[56−58] Concomitant with this observation, we assigned the $E_{red}^{(i1)}$ *and* $E_{red}^{(i2)}$ to potentials at which $[NDI]^{\bullet-}$ species and n-doped aggregates are formed. Further increase of the cathodic potentials to −1.500 V *vs* Ag/AgCl (3M KCl) initiates the formation of the dianion species, as witnessed in Figure S14. The fine vibronic structures centered at 651, 591, and 547 nm indicate that the $[NDI]^{2-}$ is molecularly dissolved.[59] To summarize, the irreversible electrochemical signals recorded for the solvated **b-NDI-(C≡CH)$_2$** units stem from noncovalent structural reorganization as schematized in Figure S15.

The potentiometric properties of the supramolecular [**b-NDI-(C≡CH)$_2$**]$_3$ constructs formed in water differ from those observed for the monomeric **b-NDI-(C≡CH)$_2$** building blocks dissolved in acetonitrile. The irreversible electrochemical signals recorded when sweeping to cathodic potentials (Figure 4A) are indicative of structural reorganization during the n-doping of the NDI noncovalent trimer. While a first inflection potential $E_{red}^{(i1)}$ is unambiguously detected at −0.380 V *vs* Ag/AgCl (3M NaCl), more complex and ill-defined signals are detected at more negative potentials. Interestingly, n-doping the [**b-NDI-(C≡CH)$_2$**]$_3$ constructs is energetically favored compared to the solvated **b-NDI-(C≡CH)$_2$** unit. This observation likely originates from the solvation environment of the supramolecular oligomer constructs. Figure S13 analyzes the spectroscopic properties of the charged species as a function of applied potentials. The rise of a broad NIR transition is observed, which reaches

https://doi.org/10.1021/acs.chemmater.3c01168
Chem. Mater. 2023, 35, 6877−6888

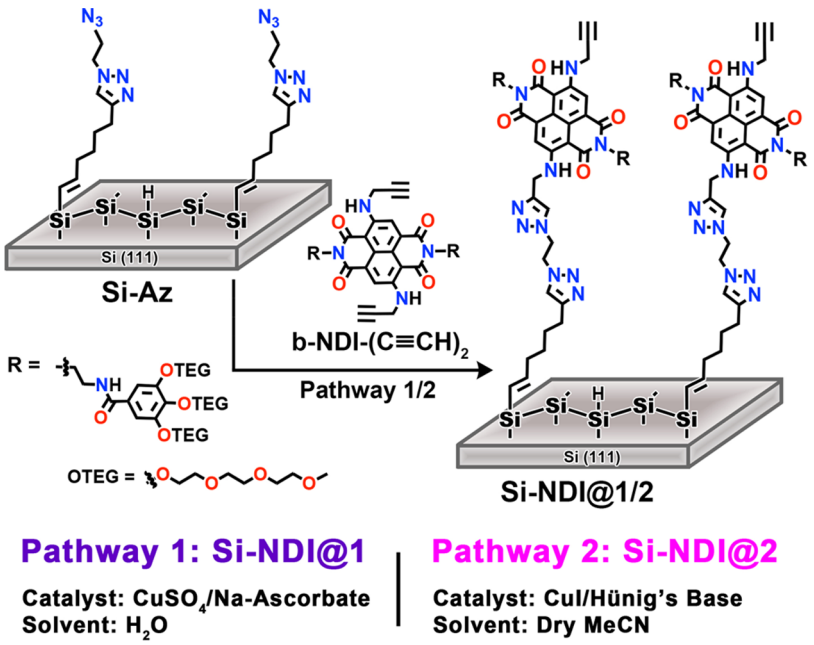

Figure 5. Synthetic access to the NDI-functionalized hybrid Si(111) interfaces **Si-NDI@1/2** based on postsynthetic modification of the azide-terminated precursor interface Si-Az with **b-NDI-(C≡CH)$_2$** via Cu^{+1}-catalyzed "click" reaction. While pathway 1 utilizes the supramolecular oligomer [**b-NDI-(C≡CH)$_2$**]$_3$ formed in aqueous medium as a reactive precursor, the molecularly dissolved parent **b-NDI-(C≡CH)$_2$** (acetonitrile) is used in pathway 2.

maximum intensity at −0.700 V *vs* Ag/AgCl (3M KCl). Further increasing the cathodic potentials to −1.100 V enforces the formation of a broad and unresolved spectroscopic feature centered at 536 nm, which does not resemble the absorptive fingerprints of the solvated NDI dianion species elucidated in CH_3CN. While a matter of speculation at this time, we hypothesize that this emergent absorption band characterizes n-doped [**b-NDI-(C≡CH)$_2$**]$_3$ constructs where more than 2 NDI units are reduced (Figure S15). Taken together, these data confirm the existence of NDI-derived noncovalent assemblies in an aqueous medium, exhibiting (opto)electronic properties that differ from those of the monomeric units solvated in CH_3CN.

Functionalization of Si Electrodes with NDI-Derived Precursors. The supramolecular [**b-NDI-(C≡CH)$_2$**]$_3$ construct and the solvated, monomeric unit **b-NDI-(C≡CH)$_2$** were anchored on Si electrodes to build semiconducting interfaces. In doing so, we aimed to demonstrate that the structures of the NDI precursors can be leveraged to control the potentiometric properties of hybrid nanointerfaces. Figure 5 summarizes the functionalization of the azide-terminated Si interface precursor (**Si-Az**)[33,60] with the [**b-NDI-(C≡CH)$_2$**]$_3$ constructs and the monomeric unit **b-NDI-(C≡CH)$_2$**, which yielded the two hybrid interfaces **Si-NDI@1** and **Si-NDI@2**, respectively. Tapping mode atomic force microscopy (AFM) was conducted to characterize the solid-state morphologies of these interfaces and probe their structural homogeneity. A representative AFM image recorded for the **Si-NDI@1** interface is shown in Figure 6A, and it uncovers that an atomically flat monolayer is constructed using "click" chemistry. Quantification of the root-mean-square roughness parameter, R_q (RMS), further validates the smoothness of the monolayers (Figure 6B) as the R_q value is below 0.5 nm.[61] These values fall in line with previous functionalized silicon-based interfaces engineered by us and others. Furthermore, the solid-state morphologies of the **Si-NDI@2** prepared using the monomeric units highlight identical solid-state morphologies and R_q values compared to the **Si-NDI@1**. Refer to Section 8 in the Supporting Information. We conclude that, at microscale dimensions, the use of supramolecular oligomers or monomeric units as reactive precursors does not alter the morphologies of the silicon interfaces.

To confirm that the NDI redox probes are indeed covalently anchored on the Si electrodes, the chemical compositions of the hybrid **Si-NDI** interfaces were investigated using high-resolution X-ray photoelectron spectroscopy (XPS). The relevant spectra for the C 1s and N 1s areas recorded with the **Si-NDI@1** are shown in Figure 6C,D. The C 1s signal (Figure 6C) for each interface can be deconvoluted into four Voigt functions at the binding energies of 287.8, 286.1, 285.6, and 284.6 eV, which are assigned to the contributions of C═O, C−O, C−N and C═C/C−C bonds, respectively. While these results may indicate covalent attachment of the NDI units onto the Si surface, C 1s signals can contain contamination from external carbon sources (C═O/C−O bonds). Consequently, the C 1s signals are corroborated with the N 1s signals to validate the covalent attachment of the redox-active NDI probes. The emission feature of the N 1s signal (Figure 6D) is deconvoluted into two Voigt functions with peaks centered at the binding energies of 401.7 and 400.3 eV, confirming the presence of chemically dissimilar nitrogen atoms. Note that identical observations are made when analyzing the **Si-NDI@2** interface. Refer to Section 9 in the Supporting Information. The combination of the C 1s and N 1s signals suggests covalent attachment of NDI redox-active units on Si electrodes, which is further confirmed by probing the potentiometric properties of the Si-NDI interfaces.

Potentiometric Properties of NDI Monolayers on Si Electrodes. The semiconducting properties of the NDI-Si interfaces are governed by the structure of the NDI precursors. Cyclic voltammetry experiments were performed using the NDI-functionalized Si hybrids as working electrodes to

https://doi.org/10.1021/acs.chemmater.3c01168
Chem. Mater. 2023, 35, 6877−6888

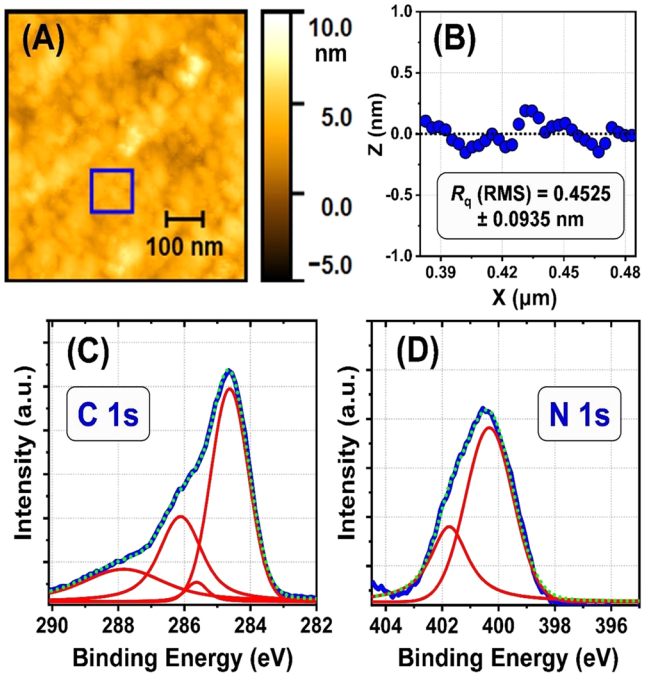

Figure 6. (A) Tapping mode AFM image of **Si-NDI@1** interface. The representative area on the AFM image designated with a blue square was probed to analyze the cross-section profile of the surface shown in (B). The R_q (RMS) surface roughness determined for the cross-section profile is noted in (B). (C, D) High-resolution XPS spectra (blue), deconvoluted spectra (red), and cumulative/sum fitted spectra (dotted green) of **Si-NDI@1**. The C 1s emission signal (C) can be deconvoluted into four Voigt functions peaking at the binding energies of 287.8, 286.1, 285.6, and 284.6 eV, which can be attributed to the contributions from C═O, C−O, C−N, and C═C/C−C bonds, respectively. The N 1s emission signal (D) can be deconvoluted into two Voigt functions with their peaks centered at the binding energies of 401.7 and 400.3 eV, confirming the presence of chemically different nitrogen atoms.

decipher the potentiometric properties of the redox-active nanointerfaces. As shown in Figure 7A, the NDI interface **Si-NDI@1** built using the supramolecular NDI oligomer exhibits well-resolved and well-defined cathodic reduction and anodic oxidation signals at a scan rate (ν) of 100 mV s^{-1}. These electrochemical signals are reversible, as indicated by the small peak-to-peak separation (ΔE_p = 50 mV) values calculated using E_p^{red} and E_p^{ox}. This behavior allows us to calculate the $E^{1/2}$ value associated with the first reduction potentials of anchored NDI (see Table S1). Furthermore, scan rate-dependent studies shown in Section 10 in the Supporting Information reveal that electrochemical reversibility (60 mV ≥ ΔE_p) is maintained up to scan rates below 150 mV s^{-1}. The potentiometric properties recorded for the **Si-NDI@2** built from molecularly dissolved NDI differ from those elucidated for the **Si-NDI@1** analog. While sweeping towards cathodic potentials, an electrochemical signal E_p^{red} is diagnosed at −0.500 V *vs* Ag/AgCl. Cycling back to anodic potentials is associated with the emergence of a more complex signal that does not resemble that recorded during the initial cathodic sweep, as illustrated in the zoom-in in Figure 7C. Indeed, a shoulder exists at a more positive potential. This electrochemical behavior unique to the **Si-NDI@2** surface suggests a non-negligible reorganization of the NDI units upon n-doping.

We provide a more accurate comparison between the reduction potential of NDI units in the **Si-NDI@1/2** interfaces by calculating the inflection-point potentials following the procedure reported by Vullev et al.[54] The inflection-point potentials $E_{red}^{(i)}$ and $E_{ox}^{(i)}$ have been assessed during the cathodic and anodic sweeps, respectively. The representative $E^{1/2}$ potential can be estimated by averaging $E_{red}^{(i)}$ and $E_{ox}^{(i)}$. Naturally, for a reversible electrochemical system, $E^{1/2}$ potential should remain constant regardless of scan rates. For details, refer to Table S3 and Figures S23−S33. It is interesting to note that while the $E^{1/2}$ calculated for the **Si-NDI@2** varies from −0.483 to −0.466 V with an average $E^{1/2}$ = −0.474 V (Figure S33), the **Si-NDI@1** nanointerface built from the NDI oligomers evidences a constant $E^{1/2}$ = −0.368 V up to a 150 mV s^{-1} scan rate (Figure S26). Note that these cyclic voltammetry experiments have been performed in an identical solvent environment and supporting electrolyte concentrations. Because the n-doping of NDI units in the **Si-NDI@1** interface is energetically favored, compared to those comprised in **Si-NDI@2**, we postulate that the conformation and chemical environments of the NDI redox units in these two interfaces must differ.

To confirm that the observed stabilization effect is an intrinsic property of covalently anchored NDI units and not the product of physisorption, we monitored the changes in the current density ($j^{(p2)}$) with increasing scan rate (Figure 7D). The current density was found to increase linearly with increasing scan rates. An excellent linear correlation is observed at lower scan rates (<200 mV s^{-1}) for both the interfaces, and the linear relationship between $j^{(p2)}$ and ν follows the classic Randles−Sevcik equation for surface-anchored redox species. This observation validates that the NDI moieties are indeed covalently attached to the surface.[62] In addition, we estimated the surface coverage of the NDI units in the **Si-NDI@1/2** interfaces by integrating the area under the capacitive-corrected cathodic peak. These calculations reveal that the surface coverages of NDI in the two hybrid interfaces are similar, with values of 1.0 ×10^{-12} and 0.61 ×10^{-12} mol cm^{-2} for **Si-NDI@1** and **Si-NDI@2**, respectively.

DFT Modeling Unravels Conformation−Energy Relationships. To assign the possible conformation adopted by NDI units in **Si-NDI@1/2** interfaces with their potentiometric properties, the two Si surfaces shown in Figure 8 were modeled using density functional theory to compute the energies of the lowest uncopied molecular orbitals. To reduce computational resources, we omitted the triazole linkers used to construct the reactive Si precursor **Si-Az** but accounted for the terminal azide functional groups. We start the discussion by justifying our hypothesis and rationale behind the choice of these model interfaces.

The **s-Si-NDI-1** model in Figure 8 is derived from NDI units connected by one covalent triazole anchor on the Si interface, placing the NDI plane in *s*-**Si-NDI-1** perpendicular with respect to the Si monolayer. This conformation is postulated to be the best representation of NDIs in the **Si-NDI@1** interface, which is constructed using the supramolecular polymer precursors. We infer that the steric hindrance imposed by the aggregate structures prevents the tethering of the NDI units via two triazoles as they lack conformational freedom of molecularly dissolved units. Indeed, the structure of the $[\mathbf{b\text{-}NDI\text{-}(C{\equiv}CH)_2}]_3$ simulated with molecular dynamics indicates the limited accessibility of the ethynyl reactive groups.

https://doi.org/10.1021/acs.chemmater.3c01168
Chem. Mater. 2023, 35, 6877−6888

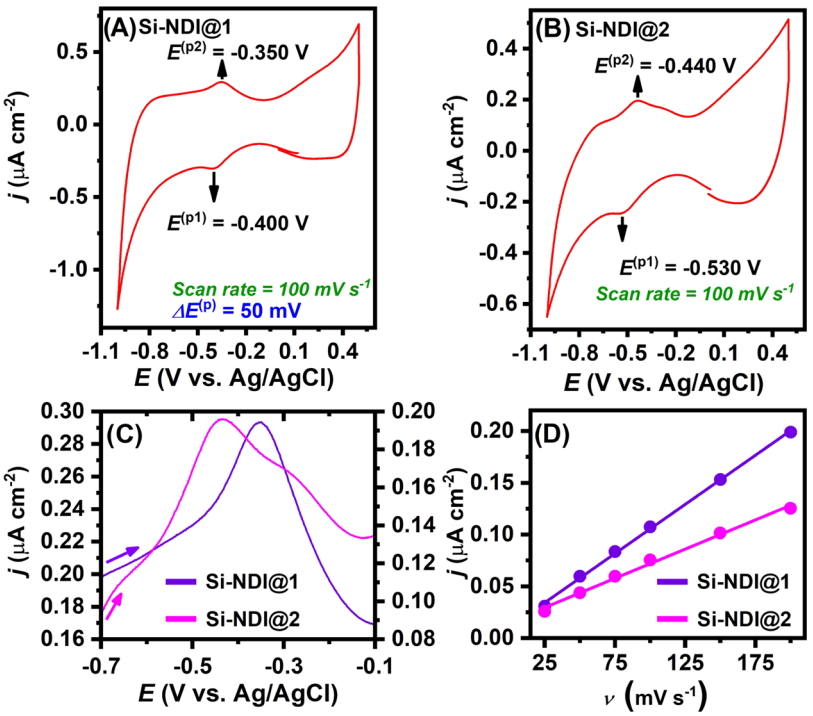

Figure 7. Cyclic voltammograms (scan rate = 100 mV s^{-1}) of **Si-NDI@1** (A) and **Si-NDI@2** (B) interfaces recorded in dry acetonitrile using 0.1 M *n*-Bu_4NPF_6 as the supporting electrolyte under Ar at 25 °C. Note that the working, reference, and counter electrodes employed for the voltammetric measurements were the Si-NDI surfaces (electroactive surface area = 0.5026 cm^2), Ag/AgCl (3 M NaCl), and Pt wire, respectively. (C) Voltametric plots (scan rate = 100 mV s^{-1}) that underscore the difference in the structural attributes of the anodic peaks in the case of **Si-NDI@1** (purple) and **Si-NDI@2** (pink) interfaces. Note that while the former exhibits a mono-component anodic peak, the latter reveals the presence of a two-component anodic peak. (D) Linear regression plots that chronicle the linear correlation of the current density, i.e., $j^{(p2)}$, of the anodic peak (i.e., p2) with scan rate (ν) for **Si-NDI@1** and **Si-NDI@2** interfaces.

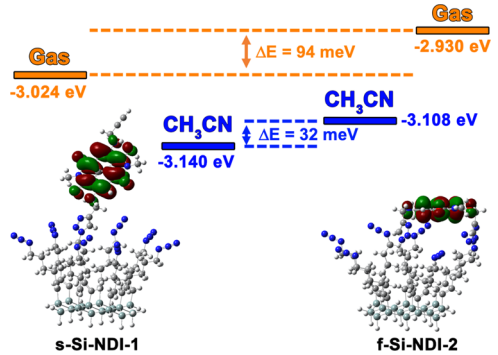

Figure 8. Energies of lowest unoccupied molecular orbitals of the two model NDI-functionalized surfaces **s-Si-NDI-1** and **f-Si-NDI-2** computed using density functional theory at the B3LYP level of theory in the gas phase and in acetonitrile using a polarization continuum model.

The **f-Si-NDI-2** model in Figure 8 features the NDI derivatives connected on the surface by two triazole moieties. This structure entails the reaction of the two propargyl groups flanked on NDI cores, which results in the NDI π-conjugated system lying flat on the reactive Si−azide precursor. We reasoned that this conformation best describes the Si interface **Si-NDI@2** built from molecularly dissolved NDI units. Specifically, following the formation of the first triazole anchor, the conformational freedom of the solvated NDI intermediates endows the second propargyl units to form the bis triazole NDI adducts.

As shown in Figure 8, the electronic density of the respective LUMO for the two model interfaces is localized on the NDI fragments. This observation confirms that the electrochemical signals experimentally measured for **Si-NDI@1/2** interfaces correspond to the n-doping of the anchored NDI units. Compellingly, the LUMO energies computed in the gas phase, and in acetonitrile, for the NDI units in the **s-Si-NDI-1** model are stabilized with respect to those computed for the f-Si-NDI-2 model. This trend parallels the stabilization of the reduction potentials experimentally measured for **Si-NDI@1** *vs.* **Si-NDI@2**. However, we note that the magnitude of the stabilization computed using DFT methods does not equal that observed experimentally. The polarizable continuum model used in our calculation does not capture the full extent of the stabilization of the NDI radical anions through interaction with acetonitrile and the supporting electrolyte.

The stabilization effect measured experimentally and supported theoretically can be rationalized by the different chemical and solvation environments experienced by the redox units in the **Si-NDI@1** *vs.* **Si-NDI@2**. The conformation of NDI in the **Si-NDI@1** interface maximizes the interaction of the π NDI core with the solvation environments as the two surfaces of the π-conjugated system are exposed. In contrast, the NDI orientation in the **Si-NDI@2** interface implies that only one face of the π-conjugated cores would interact with the solvent and supporting electrolyte. Consequently, these data indicate that the conformation of NDI in the **Si-NDI@2** monolayers enforces a larger electrostatic interaction with unreacted azides, possibly accentuating the destabilization of the NDI's LUMO energy. Furthermore, the experimentally

https://doi.org/10.1021/acs.chemmater.3c01168
Chem. Mater. 2023, 35, 6877−6888

recorded shoulder when sweeping back to positive potentials (Figure 7C) may originate from the intercalation of ammonium salts between the NDI units and the underlying azide-terminated interfaces. Similar observations have been reported for ferrocene monolayers.[15] To summarize, the combined experimental and theoretical results validate that the structure of π-conjugated supramolecular oligomers can be leveraged as a template to control the conformation of redox-active probes at Si interfaces, consequently opening new avenues to construct electronically homogeneous domains.

CONCLUSIONS

This work overcomes a long-standing challenge in electrode and nanoparticle surface engineering by reporting a new strategy to construct n-type semiconducting silicon interfaces, derived from naphthalene diimide, that exhibit reversible electrochemical processes. Specifically, we show that the restricted conformational freedom of π-conjugated cores in supramolecular constructs can be leveraged to build electronically homogeneous interfaces on silicon electrodes. Our approach relies on a novel bay-functionalized NDI unit equipped with reactive alkyne fragments. While this building block is molecularly dissolved in acetonitrile, investigating its supramolecular polymerization mechanism in an aqueous medium reveals the formation of a trimer structure in water and higher order supramolecular assemblies at larger concentrations, whose structure and electronic properties were established using MD simulation, electrochemical methods, and spectroelectrochemistry experiments. The MD-modeled trimer structures unambiguously confirm that the alkyne fragments are accessible to react. Functionalizing Si electrodes using the noncovalent NDI trimer and the molecularly dissolved analog delivers the hybrid interfaces, **Si-NDI@1** and **Si-NDI@2**, respectively, that exhibit distinct electrochemical properties. Indeed, not only is the reduction potential of the NDI units in **Si-NDI@1** stabilized by more than 100 mV with respect to that recorded with the **Si-NDI@2** interface but the interfaces derived from the supramolecular oligomer exhibit reversible electrochemical signals.

Modeling NDI-functionalized Si interfaces using DFT highlights cardinal structure−function relationships to account for when designing redox-active interfaces. While the NDI cores in **Si-NDI@2** are constrained to lay flat on the surface because of covalent anchors, the **Si-NDI@1** interface maximizes the interaction of the NDI probes with the solvation environment. All taken together, these data indicate that structurally well-defined supramolecular precursors used to functionalize Si surfaces act as conformational templates to direct the construction of electronically homogeneous interfaces. The reported strategy is a new, versatile tool to parameterize the conformation of π-conjugated chromophores interfacing with inorganic (semi)conducting substrates. Structurally and electronically well-defined nanointerfaces derived from redox-active rylene diimide units open new avenues to engineer heterogeneous photocatalyst systems, (bio)chemical sensors, and light-harvesting materials primed for photon upconversion capabilities.

MATERIALS AND METHODS

Materials. Unless otherwise mentioned, all chemicals were used as received. All air-sensitive reagents were handled in a Braun Labmaster DP glovebox. Standard Schlenk techniques were utilized to handle air-sensitive solutions. Acetonitrile (MeCN) was dried over $CaCl_2$ and distilled under argon. Deuterated solvents used for preparing solutions for NMR spectra acquisition were used as received from Cambridge Isotope Laboratories. Compounds 1,4,5,8-naphthalenetetracarboxylic dianhydride, ethylenediamine, triethylene glycol monomethyl ether, *N*-hydroxysuccinimide, and propargylamine were purchased from Tokyo Chemical Industry and used without further purification. Compound 4-toluenesulfonyl chloride was purchased from Alfa Aesar. All solvents used for synthesis, purification (ACS grade), and data acquisition (HPLC grade), namely, dichloromethane (DCM), *N*,*N*-dimethylformamide (DMF), acetone, methanol (MeOH), 2-methoxyethanol, water, etc., were purchased from VWR. Solvents used were dehydrated and stored over activated molecular sieves.

Synthesis of the b-NDI-(C≡CH)$_2$ Building Block. In a 100 mL dry Schlenk flask equipped with a magnetic stir bar, 118 mg (0.069 mmol) of NDI-$(Br)_2$-$(C_2GA)_2$ were placed under argon atmosphere. Subsequently, 20 mL of dry 2-methoxyethanol is cannulated into the flask, and 167 μL (0.906 mmol) of propargylamine is added to the solution dropwise. The solution is heated at 140 °C for 24 h. After the reaction was completed, the volatiles were evaporated, and the compound was first subjected to silicon flash chromatography using an eluent of 90% DCM, 5% MeOH, and 5% TEA. The product was further purified utilizing HPLC with a reverse phase column (Biotage Sfär Bio C18 D cartridge Duo 300 Å 20 μm) and an eluent of 1:1.5 H_2O to MeCN. After combining the pure fractions and evaporating the volatiles under vacuum, the compound was isolated as a waxy deep blue solid (50 mg, 43.8%). ^{1}H NMR (400 MHz, $CDCl_3$) δ 8.27 (s, 2H), 7.06 (s, 4H), 4.52 (d, *J* = 6.3 Hz, 4H), 4.33 (dd, *J* = 6.0, 2.4 Hz, 4H), 4.20 (q, *J* = 4.6 Hz, 12H), 3.86 (t, *J* = 5.0 Hz, 11H), 3.80 (t, *J* = 5.1 Hz, 5H), 3.73 (dt, *J* = 5.6, 3.3 Hz, 11H), 3.65 (qd, *J* = 4.9, 3.0 Hz, 24H), 3.55 (dd, *J* = 5.6, 3.5 Hz, 12H), 3.38 (d, *J* = 4.3 Hz, 18H), 2.40 (q, *J* = 3.2 Hz, 2H). ^{13}C NMR (101 MHz, $CDCl_3$) δ 167.05, 166.52, 152.38, 148.63, 129.42, 121.63, 106.84, 102.97, 78.89, 77.32, 77.00, 76.68, 72.96, 72.34, 71.93, 71.91, 70.74, 70.65, 70.63, 70.54, 70.50, 70.47, 69.66, 68.87, 58.99, 58.98, 32.65, 29.69. ESI-MS$^+$ *m*/*z* calcd for $C_{80}H_{114}N_6O_{30}$ 1662.8 [M + Na], found 1662.775.

Diffusion-Ordered NMR Spectroscopy (DOSY). ^{1}H-DOSY NMR experiments were carried out at 25 °C in a Bruker Avance 400 MHz NMR spectrometer. For the ^{1}H-DOSY experiments, 64 scans were obtained, utilizing a diffusion time of 200 ms for the monomeric state and 450 ms for the oligomeric state. A p19 time of 500 μs and a p30 of 1 ms were used for all measurements, as well as a pulse gradient of 5−95%. Hydrodynamic radii for the monomer ($R_{h,mon}$) and the supramolecular oligomer ($R_{h,SO}$) were determined by using the Stokes-Einstein Gierer-Wirtz Estimation (SEGWE).[63] The number of monomer units within the supramolecular oligomer was estimated as $N \approx (R_{h,SO}/R_{h,mon})^3$.[64]

Molecular Dynamics Simulations. Structures of **b-NDI-(C≡CH)$_2$** aggregates were generated using a modified top-down approach—"the building-up method": a unimer, modeled using UCSF Chimera,[65] was relaxed using a 10 ns NPT run. The resulting structure from this trajectory was then duplicated and used to create a preordered dimer with an interfacial distance of 5 nm between NDI cores, which was then run using a 200 ns NPT simulation. The K-means[66] clustering algorithm (using 10 clusters) was then utilized to find the dominant state of this dimer during the production run—this dominant cluster was then used to create a trimer, also simulated for a 200 ns *NPT* run. Density mapping of the carbon and oxygen atoms of **b-NDI-(C≡CH)$_2$** ethylene glycol chains was performed over the course of the simulation trajectories using cpptraj, with the resulting grids visualized using UCSF Chimera.

Solution-State Electrochemistry and Spectroelectrochemistry of b-NDI-(C≡CH)$_2$. Cyclic voltammograms were recorded on a PARSTAT 3000A potentiostat (Ametek Scientific Instruments, USA) using a standard electrochemical cell for the solutions (concentration = 200 μM) of **b-NDI-(C≡CH)$_2$** in H_2O (supporting electrolyte = 0.1 M NaCl) and dry MeCN (supporting electrolyte = 0.1 M *n*-Bu_4NPF_6) under Ar gas atmosphere at 25 °C. The voltammograms were recorded using glassy carbon as the working electrode (electroactive surface area = 0.071 cm^2), Ag/AgCl (3 M NaCl) as the reference electrode, and Pt as the counter electrode. Note that $E^{(p)}$

https://doi.org/10.1021/acs.chemmater.3c01168
Chem. Mater. 2023, 35, 6877−6888

and $E^{(i)}$ refer to the potentials of the cathodic/anodic peak and the potentials at the inflection points of the cathodic waves (as determined from the first derivative plots), respectively. Further note that all of the potentials are referenced with respect to Ag/AgCl (3M NaCl) electrode, which was standardized during each measurement using ferrocene as the standard. Spectroelectrochemistry measurements were carried out using a PARSTAT 3000A potentiostat (Ametek Scientific Instruments, USA) and a Cary 5000 UV−vis-NIR spectrophotometer. In a typical experiment, a solution (concentration ∼ 500 μM, OD ∼ 2.5, l = 1.70 mm) of an NDI derivative in D_2O or CH_3CN was gently degassed in a 1.70 mm pathlength modified quartz cell. The cell was equipped with an Au honeycomb electrode that serves both as the working and counter electrodes and a reference electrode (Ag/AgCl, 3 M NaCl). Prior to taking all reported spectra, the potentials were equilibrated for about 10 minutes, or until the applied current plateaued to the smallest possible current (typically I < −200 μA). All experiments were conducted under a gentle flow of Ar to prevent oxygen and water contamination. Subsequently, the ground-state electronic absorption spectrum of the NDI solution was recorded, followed by a gradual increase in the applied cathodic reduction potential (i.e., more negative) in intervals of 50 mV until achievement of the endpoint of the experiment.

XPS Characterization Data. The chemical compositions of the hybrid **Si-NDI** interfaces were interrogated using XPS as the characterization tool. The XPS data were recorded on a Kratos Axis Ultra DLD system equipped with an Al Kα monochromatic source and a base pressure of ca. 6×10^{-9} torr. The survey (full) and the high-resolution spectra were collected at the pass energies of 80 and 20 eV, respectively. A charge neutralizer was employed for the charge compensation, and notably, all of the data was corrected to the C 1s peak at the binding energy of 284.6 eV.

Potentiometric Properties of the Si-NDI@1/2 Interface. The potentiometric properties of **Si-NDI@1/2** interfaces were investigated by scan rate-dependent cyclic voltammograms recorded on a PARSTAT 3000A potentiostat (Ametek Scientific Instruments). The CVs were recorded using a custom-made three-electrode Teflon cell using **Si-NDI @1/2** interfaces as the working electrodes (electroactive surface area = 0.5026 cm^2), Ag/AgCl (3 M NaCl) as the reference electrode (standardized and calibrated with ferrocene), and Pt wire as the counter electrode using n-Bu_4NPF_6 (0.1 M) as the supporting electrolyte in dry MeCN under Ar at 25 °C.

DFT Calculations. Structure optimization calculations were performed using density functional theory (DFT) in the Gaussian 09.D01 software package. The B3LYP hybrid density functional theory model, in combination with the 6-311g(d) basis set, was exploited to model all of the surfaces. To prevent convergence issues, an incremental stepwise approach was used to minimize the final truncated surfaces that feature the NDI units. In the first step, an initial Si−H surface Si(111) built from 16 Si atoms was minimized and is shown in Figure S38. In the second step, the alkene-functionalized surface Si−alkene shown in Figure S38 was minimized by freezing the Si layers. The third step minimized the alkyl-terminated Si precursor Si−alkyl shown in Figure S38, where the Si−C═CH functions have been frozen. The azide−terminate Si surface Si−azide was minimized by freezing the Si−C═$CHCH_2CH_2CH_2$ fragments. Finally, the s-SI-NDI-1 and f-Si-NDI-2 are constructed from the Si−azide precursors and minimized in the gas phase using the Si−C═$CHCH_2CH_2CH_2$ as frozen fragments. For the calculation of the LUMO energies in acetonitrile solvent, a polarized continuum solvation model (SCRF = IEF PCM) with acetonitrile as the solvent was used.

■ ASSOCIATED CONTENT

Supporting Information

The Supporting Information is available free of charge at https://pubs.acs.org/doi/10.1021/acs.chemmater.3c01168.

Synthesis and characterization of the **b-NDI-(C≡CH)$_2$** building block, supramolecular polymerization mechanism, 2D NMR spectroscopy, electrochemistry, spectroelectrochemistry, XPS, atomic force microscopy, molecular dynamics simulation, DFT calculation, and 1D NMR and high-resolution MS (PDF)

■ AUTHOR INFORMATION

Corresponding Authors

Arindam Mukhopadhyay − *Department of Chemistry, The University of Miami, Coral Gables 33124-0431 Florida, United States;* Present Address: Chemical Systems Department, Energy and Environment Science and Technology Division, Idaho National Laboratory, Battelle Energy Alliance, United States Department of Energy, 1955 N Fremont Avenue, Idaho Falls, Idaho 83415; orcid.org/0000-0002-0620-4157; Phone: +1-208-526-5137; Email: Arindam.Mukhopadhyay@inl.gov

Jean-Hubert Olivier − *Department of Chemistry, The University of Miami, Coral Gables 33124-0431 Florida, United States;* orcid.org/0000-0003-0978-4107; Phone: +1-305-284-3279; Email: jh.olivier@miami.edu

Authors

Ifigeneia Tsironi − *Department of Chemistry, The University of Miami, Coral Gables 33124-0431 Florida, United States*

Jarek A. Maleszka − *Department of Chemistry, The University of Miami, Coral Gables 33124-0431 Florida, United States*

Robert S. Wilson-Kovacs − *Department of Chemistry, The University of Miami, Coral Gables 33124-0431 Florida, United States*

Victor A. Paulino − *Department of Chemistry, The University of Miami, Coral Gables 33124-0431 Florida, United States;* orcid.org/0000-0001-8916-3604

Orlando Acevedo − *Department of Chemistry, The University of Miami, Coral Gables 33124-0431 Florida, United States;* orcid.org/0000-0002-6110-3930

Complete contact information is available at: https://pubs.acs.org/10.1021/acs.chemmater.3c01168

Author Contributions

The manuscript was written with the contributions of all authors. All authors have approved the final version of the manuscript.

Funding

The research conducted on the synthesis and aggregation properties of π-conjugated dyes is supported by the National Science Foundation through the NSF CAREER award CHE-1941410. Efforts related to the functionalization of silicon electrodes are sponsored by the Arnold and Mabel Beckman Foundation through the Arnold and Mabel Beckman Young Investigator Award 2018.

Notes

The authors declare no competing financial interest.

■ ACKNOWLEDGMENTS

The authors thank Dr. Carrie Donley at UNC Chapel Hill for performing XPS experiments on the functionalized surface. They are grateful to BioNIUM for providing access to the atomic force microscope. They also thank Dr. Ziming Zhang in the Department of Chemistry at the University of Miami for providing guidance on the 2D NMR experiments. The authors are grateful to the Institute for Data Science and Computing at the University of Miami for providing access to Pegasus supercomputer.

REFERENCES

(1) Polizzi, N. F.; Eibling, M. J.; Perez-Aguilar, J. M.; Rawson, J.; Lanci, C. J.; Fry, H. C.; Beratan, D. N.; Saven, J. G.; Therien, M. J. Photoinduced electron transfer elicits a change in the static dielectric constant of a de novo designed protein. *J. Am. Chem. Soc.* **2016**, *138*, 2130−2133.

(2) Kim, D.; Kim, J.; Lee, T. S. Photoswitchable chromic behavior of conjugated polymer films for reversible patterning and construction of a logic gate. *Polym. Chem.* **2017**, *8*, 5539−5545.

(3) Yu, J.; Park, J.; Van Wyk, A.; Rumbles, G.; Deria, P. Excited-state electronic properties in Zr-based metal−organic frameworks as a function of a topological network. *J. Am. Chem. Soc.* **2018**, *140*, 10488−10496.

(4) Khusnutdinova, D.; Beiler, A.; Wadsworth, B.; Jacob, S.; Moore, G. Metalloporphyrin-modified semiconductors for solar fuel production. *Chem. Sci.* **2017**, *8*, 253−259.

(5) Bullard, G.; Tassinari, F.; Ko, C.-H.; Mondal, A. K.; Wang, R.; Mishra, S.; Naaman, R.; Therien, M. J. Low-resistance molecular wires propagate spin-polarized currents. *J. Am. Chem. Soc.* **2019**, *141*, 14707−14711.

(6) Song, R.; Wang, Z.; Zhou, X.; Huang, L.; Chi, L. Gas-Sensing Performance and Operation Mechanism of Organic π-Conjugated Materials. *ChemPlusChem* **2019**, *84*, 1222−1234.

(7) Schroeder, V.; Savagatrup, S.; He, M.; Lin, S.; Swager, T. M. Carbon Nanotube Chemical Sensors. *Chem. Rev.* **2019**, *119*, 599−663.

(8) Mativetsky, J. M.; Orgiu, E.; Lieberwirth, I.; Pisula, W.; Samorì, P. Charge transport over multiple length scales in supramolecular fiber transistors: Single fiber versus ensemble performance. *Adv. Mater.* **2014**, *26*, 430−435.

(9) Di Nuzzo, D.; Kulkarni, C.; Zhao, B.; Smolinsky, E.; Tassinari, F.; Meskers, S. C.; Naaman, R.; Meijer, E.; Friend, R. H. High circular polarization of electroluminescence achieved via self-assembly of a light-emitting chiral conjugated polymer into multidomain cholesteric films. *ACS Nano* **2017**, *11*, 12713−12722.

(10) Deria, P.; Olivier, J.-H.; Park, J.; Therien, M. J. Potentiometric, Electronic, and Transient Absorptive Spectroscopic Properties of Oxidized Single-Walled Carbon Nanotubes Helically Wrapped by Ionic, Semiconducting Polymers in Aqueous and Organic Media. *J. Am. Chem. Soc.* **2014**, *136*, 14193−14199.

(11) Ciampi, S.; Eggers, P. K.; Le Saux, G.; James, M.; Harper, J. B.; Gooding, J. J. Silicon (100) electrodes resistant to oxidation in aqueous solutions: an unexpected benefit of surface acetylene moieties. *Langmuir* **2009**, *25*, 2530−2539.

(12) Fabre, B. Ferrocene-Terminated Monolayers Covalently Bound to Hydrogen-Terminated Silicon Surfaces. Toward the Development of Charge Storage and Communication Devices. *Acc. Chem. Res.* **2010**, *43*, 1509−1518.

(13) Mukhopadhyay, A.; Paulino, V.; Liu, K.; Donley, C. L.; Bernard, B.; Shomar, A.; Liu, C.; Olivier, J.-H. Leveraging the Assembly of a Rylene Dye to Tune the Semiconducting Properties of Functionalized n-Type, Hybrid Si Interfaces. *ACS Appl. Mater. Interfaces* **2021**, *13*, 4665−4675.

(14) Park, J.; Belding, L.; Yuan, L.; Mousavi, M. P. S.; Root, S. E.; Yoon, H. J.; Whitesides, G. M. Rectification in Molecular Tunneling Junctions Based on Alkanethiolates with Bipyridine−Metal Complexes. *J. Am. Chem. Soc.* **2021**, *143*, 2156−2163.

(15) Wong, R. A.; Yokota, Y.; Wakisaka, M.; Inukai, J.; Kim, Y. Discerning the Redox-Dependent Electronic and Interfacial Structures in Electroactive Self-Assembled Monolayers. *J. Am. Chem. Soc.* **2018**, *140*, 13672−13679.

(16) Wadsworth, B. L.; Beiler, A. M.; Khusnutdinova, D.; Jacob, S. I.; Moore, G. F. Electrocatalytic and Optical Properties of Cobaloxime Catalysts Immobilized at a Surface-Grafted Polymer Interface. *ACS Catal.* **2016**, *6*, 8048−8057.

(17) Boucher, D. G.; Kearney, K.; Ertekin, E.; Rose, M. J. Tuning p-Si(111) Photovoltage via Molecule|Semiconductor Electronic Coupling. *J. Am. Chem. Soc.* **2021**, *143*, 2567−2580.

(18) Tachikawa, T.; Cui, S.-C.; Tojo, S.; Fujitsuka, M.; Majima, T. Nanoscopic heterogeneities in adsorption and electron transfer processes of perylene diimide dye on TiO2 nanoparticles studied by single-molecule fluorescence spectroscopy. *Chem. Phys. Lett.* **2007**, *443*, 313−318.

(19) Brennaman, M. K.; Norris, M. R.; Gish, M. K.; Grumstrup, E. M.; Alibabaei, L.; Ashford, D. L.; Lapides, A. M.; Papanikolas, J. M.; Templeton, J. L.; Meyer, T. J. Ultrafast, Light-Induced Electron Transfer in a Perylene Diimide Chromophore-Donor Assembly on TiO2. *J. Phys. Chem. Lett.* **2015**, *6*, 4736−4742.

(20) Li, C.; Wonneberger, H. Perylene Imides for Organic Photovoltaics: Yesterday, Today, and Tomorrow. *Adv. Mater.* **2012**, *24*, 613−636.

(21) Wei, W.; Zhu, Y. TiO2@Perylene Diimide Full-Spectrum Photocatalysts via Semi-Core−Shell Structure. *Small* **2019**, *15*, No. 1903933.

(22) Xia, P.; Raulerson, E. K.; Coleman, D.; Gerke, C. S.; Mangolini, L.; Tang, M. L.; Roberts, S. T. Achieving spin-triplet exciton transfer between silicon and molecular acceptors for photon upconversion. *Nat. Chem.* **2020**, *12*, 137−144.

(23) Huang, T.; Koh, T. T.; Schwan, J.; Tran, T. T. T.; Xia, P.; Wang, K.; Mangolini, L.; Tang, M. L.; Roberts, S. T. Bidirectional triplet exciton transfer between silicon nanocrystals and perylene. *Chem. Sci.* **2021**, *12*, 6737−6746.

(24) Hauquier, F.; Ghilane, J.; Fabre, B.; Hapiot, P. Conducting Ferrocene Monolayers on Nonconducting Surfaces. *J. Am. Chem. Soc.* **2008**, *130*, 2748−2749.

(25) Fabre, B.; Pujari, S. P.; Scheres, L.; Zuilhof, H. Micropatterned Ferrocenyl Monolayers Covalently Bound to Hydrogen-Terminated Silicon Surfaces: Effects of Pattern Size on the Cyclic Voltammetry and Capacitance Characteristics. *Langmuir* **2014**, *30*, 7235−7243.

(26) Zhang, L.; Vogel, Y. B.; Noble, B. B.; Gonçales, V. R.; Darwish, N.; Brun, A. L.; Gooding, J. J.; Wallace, G. G.; Coote, M. L.; Ciampi, S. TEMPO Monolayers on Si(100) Electrodes: Electrostatic Effects by the Electrolyte and Semiconductor Space-Charge on the Electroactivity of a Persistent Radical. *J. Am. Chem. Soc.* **2016**, *138*, 9611−9619.

(27) Gooding, J. J.; Ciampi, S. The molecular level modification of surfaces: from self-assembled monolayers to complex molecular assemblies. *Chem. Soc. Rev.* **2011**, *40*, 2704−2718.

(28) Tian, F.; Teplyakov, A. V. Silicon Surface Functionalization Targeting Si−N Linkages. *Langmuir* **2013**, *29*, 13−28.

(29) Itoh, Y.; Kim, B.; Gearba, R. I.; Tremblay, N. J.; Pindak, R.; Matsuo, Y.; Nakamura, E.; Nuckolls, C. Simple Formation of C60 and C60-Ferrocene Conjugated Monolayers Anchored onto Silicon Oxide with Five Carboxylic Acids and Their Transistor Applications. *Chem. Mater.* **2011**, *23*, 970−975.

(30) Liu, Z.; Yasseri, A. A.; Loewe, R. S.; Lysenko, A. B.; Malinovskii, V. L.; Zhao, Q.; Surthi, S.; Li, Q.; Misra, V.; Lindsey, J. S.; Bocian, D. F. Synthesis of Porphyrins Bearing Hydrocarbon Tethers and Facile Covalent Attachment to Si(100). *J. Org. Chem.* **2004**, *69*, 5568−5577.

(31) Feng, W.; Miller, B. J. E. Fullerene Monolayer-Modified Porous Si. Synthesis and Photoelectrochemistry. *Electrochem. Solid-State Lett.* **1999**, *1*, No. 172.

(32) Errington, R. J.; Petkar, S. S.; Horrocks, B. R.; Houlton, A.; Lie, L. H.; Patole, S. N. Covalent Immobilization of a TiW5 Polyoxometalate on Derivatized Silicon Surfaces. *Angew. Chem., Int. Ed.* **2005**, *44*, 1254−1257.

(33) Mukhopadhyay, A.; Liu, K.; Paulino, V.; Olivier, J.-H. Modulating the Conduction Band Energies of Si Electrode Interfaces Functionalized with Monolayers of a Bay-Substituted Perylene Bisimide. *Langmuir* **2022**, *38*, 4266−4275.

(34) Fabre, B. Functionalization of Oxide-Free Silicon Surfaces with Redox-Active Assemblies. *Chem. Rev.* **2016**, *116*, 4808−4849.

(35) Volatron, F.; Noël, J.-M.; Rinfray, C.; Decorse, P.; Combellas, C.; Kanoufi, F.; Proust, A. Electron transfer properties of a monolayer of hybrid polyoxometalates on silicon. *J. Mater. Chem. C* **2015**, *3*, 6266−6275.

https://doi.org/10.1021/acs.chemmater.3c01168
Chem. Mater. 2023, 35, 6877−6888

(36) Vadehra, G. S.; Maloney, R. P.; Garcia-Garibay, M. A.; Dunn, B. Naphthalene Diimide Based Materials with Adjustable Redox Potentials: Evaluation for Organic Lithium-Ion Batteries. *Chem. Mater.* **2014**, *26*, 7151−7157.
(37) Al Kobaisi, M.; Bhosale, S. V.; Latham, K.; Raynor, A. M.; Bhosale, S. V. Functional naphthalene diimides: synthesis, properties, and applications. *Chem. Rev.* **2016**, *116*, 11685−11796.
(38) Quinn, S.; Davies, E. S.; Pfeiffer, C. R.; Lewis, W.; McMaster, J.; Champness, N. R. Core-Substituted Naphthalene Diimides: Influence of Substituent Conformation on Strong Visible Absorption. *ChemPlusChem* **2017**, *82*, 489−492.
(39) Sakai, N.; Mareda, J.; Vauthey, E.; Matile, S. Core-substituted naphthalenediimides. *Chem. Commun.* **2010**, *46*, 4225−4237.
(40) Bhosale, S. V.; Bhosale, S. V.; Bhargava, S. K. Recent progress of core-substituted naphthalenediimides: highlights from 2010. *Org. Biomol. Chem.* **2012**, *10*, 6455−6468.
(41) Isukapalli, S. V. K.; Pushparajan, P.; Vennapusa, S. R. Rationalizing the Fluorescence Behavior of Core-Substituted Naphthalene Diimides. *J. Phys. Chem. A* **2022**, *126*, 1114−1122.
(42) Mukherjee, A.; Sakurai, T.; Seki, S.; Ghosh, S. Naphthalenediimide (NDI)-Conjugated Foldable Polyurethanes: Impact of Chromophoric Location on Hierarchical Supramolecular Assembly and Conductivity. *ChemNanoMat* **2018**, *4*, 860−866.
(43) Chakraborty, D.; Sarkar, D.; Ghosh, A. K.; Das, P. K. Lipase sensing by naphthalene diimide based fluorescent organic nanoparticles: a solvent induced manifestation of self-assembly. *Soft Matter* **2021**, *17*, 2170−2180.
(44) Hestand, N. J.; Spano, F. C. Expanded Theory of H- and J-Molecular Aggregates: The Effects of Vibronic Coupling and Intermolecular Charge Transfer. *Chem. Rev.* **2018**, *118*, 7069−7163.
(45) Kar, H.; Ghosh, G.; Ghosh, S. Solvent Geometry Regulated Cooperative Supramolecular Polymerization. *Chem. - Eur. J.* **2017**, *23*, 10536−10542.
(46) Kar, H.; Gehrig, D. W.; Allampally, N. K.; Fernández, G.; Laquai, F.; Ghosh, S. Cooperative supramolecular polymerization of an amine-substituted naphthalene-diimide and its impact on excited state photophysical properties. *Chem. Sci.* **2016**, *7*, 1115−1120.
(47) Paulino, V.; Mukhopadhyay, A.; Tsironi, I.; Liu, K.; Husainy, D.; Liu, C.; Meier, K.; Olivier, J.-H. Molecular Engineering of Water-Soluble Oligomers to Elucidate Radical π−Anion Interactions in n-Doped Nanoscale Objects. *J. Phys. Chem. C* **2021**, *125*, 10526−10538.
(48) Korevaar, P. A.; Schaefer, C.; de Greef, T. F. A.; Meijer, E. W. Controlling Chemical Self-Assembly by Solvent-Dependent Dynamics. *J. Am. Chem. Soc.* **2012**, *134*, 13482−13491.
(49) Kotha, S.; Mabesoone, M. F. J.; Srideep, D.; Sahu, R.; Reddy, S. K.; Rao, K. V. Supramolecular Depolymerization in the Mixture of Two Poor Solvents: Mechanistic Insights and Modulation of Supramolecular Polymerization of Ionic π-Systems. *Angew. Chem., Int. Ed.* **2021**, *60*, 5459−5466.
(50) Paulino, V.; Liu, K.; Cesiliano, V.; Tsironi, I.; Mukhopadhyay, A.; Kaufman, M.; Olivier, J.-H. Covalent post-assembly modification of π-conjugated supramolecular polymers delivers structurally robust light-harvesting nanoscale objects. *Nanoscale* **2023**, *15*, 4448−4456.
(51) Ogi, S.; Stepanenko, V.; Sugiyasu, K.; Takeuchi, M.; Würthner, F. Mechanism of Self-Assembly Process and Seeded Supramolecular Polymerization of Perylene Bisimide Organogelator. *J. Am. Chem. Soc.* **2015**, *137*, 3300−3307.
(52) Tan, M.; Takeuchi, M.; Takai, A. Spatiotemporal dynamics of supramolecular polymers by in situ quantitative catalyst-free hydroamination. *Chem. Sci.* **2022**, *13*, 4413−4423.
(53) Syamala, P. P. N.; Würthner, F. Modulation of the Self-Assembly of π-Amphiphiles in Water from Enthalpy- to Entropy-Driven by Enwrapping Substituents. *Chem. - Eur. J.* **2020**, *26*, 8426−8434.
(54) Espinoza, E. M.; Clark, J. A.; Soliman, J.; Derr, J. B.; Morales, M.; Vullev, V. I. Practical aspects of cyclic voltammetry: how to estimate reduction potentials when irreversibility prevails. *J. Electrochem. Soc.* **2019**, *166*, H3175−H3187.
(55) Röger, C.; Würthner, F. Core-Tetrasubstituted Naphthalene Diimides: Synthesis, Optical Properties, and Redox Characteristics. *J. Org. Chem.* **2007**, *72*, 8070−8075.
(56) Penneau, J. F.; Stallman, B. J.; Kasai, P. H.; Miller, L. L. An imide anion radical that dimerizes and assembles into.pi.-stacks in solution. *Chem. Mater.* **1991**, *3*, 791−796.
(57) Liu, K.; Levy, A.; Liu, C.; Olivier, J.-H. Tuning Structure−Function Properties of π-Conjugated Superstructures by Redox-Assisted Self-Assembly. *Chem. Mater.* **2018**, *30*, 2143−2150.
(58) Liu, K.; Paulino, V.; Mukhopadhyay, A.; Bernard, B.; Kumbhar, A.; Liu, C.; Olivier, J.-H. How to reprogram the excitonic properties and solid-state morphologies of π-conjugated supramolecular polymers. *Phys. Chem. Chem. Phys.* **2021**, *23*, 2703−2714.
(59) Gosztola, D.; Niemczyk, M. P.; Svec, W.; Lukas, A. S.; Wasielewski, M. R. Excited Doublet States of Electrochemically Generated Aromatic Imide and Diimide Radical Anions. *J. Phys. Chem. A* **2000**, *104*, 6545−6551.
(60) Mukhopadhyay, A.; Liu, K.; Paulino, V.; Donley, C. L.; Olivier, J.-H. Silicon Electrodes Functionalized with Perylene Bisimide π-Aggregates for Redox-Controlled Stabilization of Semiconducting Nanointerfaces. *ACS Appl. Nano Mater* **2021**, *4*, 8813−8822.
(61) Ranganathan, S.; McCreery, R. L. Electroanalytical Performance of Carbon Films with Near-Atomic Flatness. *Anal. Chem.* **2001**, *73*, 893−900.
(62) Elgrishi, N.; Rountree, K. J.; McCarthy, B. D.; Rountree, E. S.; Eisenhart, T. T.; Dempsey, J. L. A Practical Beginner's Guide to Cyclic Voltammetry. *J. Chem. Edu.* **2018**, *95*, 197−206.
(63) Evans, R.; Dal Poggetto, G.; Nilsson, M.; Morris, G. A. J. A. c. Improving the interpretation of small molecule diffusion coefficients. *Anal. Chem.* **2018**, *90*, 3987−3994.
(64) Herkert, L.; Droste, J.; Kartha, K. K.; Korevaar, P. A.; de Greef, T. F.; Hansen, M. R.; Fernández, G. J. A. C. Pathway Control in Cooperative vs. Anti-Cooperative Supramolecular Polymers. *Angew. Chem., Int. Ed.* **2019**, *131*, 11466−11471.
(65) Pettersen, E. F.; Goddard, T. D.; Huang, C. C.; Couch, G. S.; Greenblatt, D. M.; Meng, E. C.; Ferrin, T. E. UCSF Chimera—A visualization system for exploratory research and analysis. *J. Comput. Chem.* **2004**, *25*, 1605−1612.
(66) MacQueen, J.*Some Methods for Classification and Analysis of Multivariate Observations*, Berkeley Symposium on Mathematical Statistics and Probability, 1967; pp 281−297.

https://doi.org/10.1021/acs.chemmater.3c01168
Chem. Mater. 2023, 35, 6877−6888